atmosphere

Article

Comparison of Atmospheric Turbulence Characteristics over Sea Surface and Land Surface before, during, and after Typhoons

Xueyan Bi [1], Chao Lu [2], Chunxia Liu [1,*], Jian Huang [1], Honglong Yang [2], Zhongkuo Zhao [1] and Qingtao Song [1]

1 Guangdong Provincial Key Laboratory of Regional Numerical Weather Prediction, Guangzhou Institute of Tropical and Marine Meteorology, China Meteorological Administration, Guangzhou 510080, China
2 Shenzhen National Climate Observatory, Shenzhen 518038, China
* Correspondence: cxliu@gd121.cn

Abstract: The goal of the paper is to reveal discrepancies of turbulent variables over different surfaces (sea, island, land) based on the measurements taken on three towers during (including before and after) seven typhoon episodes from 2008 to 2018. The atmospheric stability, turbulent spectrum, friction velocity, turbulent kinetic energy, dissipative heating, and gust factor are examined. The similar turbulent characteristics over sea and on the island reinforce the previous conclusion that the turbulent measurements on the island mainly represent the sea surface. The turbulent characteristics over sea and on land are very different due to the different underlying surface roughness. The unstable (stable) condition dominates on the sea (land) surface. Turbulent spectra both over sea and on land follow the canonical Kolmogorov's power law with the −5/3 slope. The cospectra on land are more peaked than those over sea. All of the friction velocity, turbulent kinetic energy, and dissipative heating increase with increasing 10 m wind speed, and those on land are much larger than those over sea. The distributions of gust factors widen and shift to higher on land than those over sea. The distributions of gust factors at heights of 10 m and 40 m are biased to higher values than those at heights of 160 m and 320 m on land.

Keywords: underlying surface; typhoon; atmospheric stability; turbulent spectra; turbulent kinetic energy; dissipative heating; gust factor

check for updates

Citation: Bi, X.; Lu, C.; Liu, C.; Huang, J.; Yang, H.; Zhao, Z.; Song, Q. Comparison of Atmospheric Turbulence Characteristics over Sea Surface and Land Surface before, during, and after Typhoons. *Atmosphere* **2022**, *13*, 1827. https://doi.org/10.3390/atmos13111827

Academic Editor: Luca Mortarini

Received: 24 August 2022
Accepted: 31 October 2022
Published: 3 November 2022

1. Introduction

Turbulence fluctuations in the atmospheric surface layer have a significant effect on various applications including wind loads; aviation; design codes for bridges, buildings, and electrical transmission lines; and resuspension models for deposited particles [1,2]. It is well known that the structure of atmospheric turbulence in the surface layer is closely related to surface roughness. There are different processes of turbulent exchanges on different underlying surfaces. Compared with the sea surface, the land surface is more rough, heterogeneous, and complex [3,4].

Some previous studies compared turbulent variables over different surfaces, such as atmospheric stability, spectra, gust factor, etc. They showed that the marine air below 50 m is in mostly unstable and neutral conditions [5,6]. The gust factor is sensitive to surface roughness and turbulent intensity [1,7]. The power spectra in the region of the inertial subrange with decay of −5/3 appears over lakes and forest [4]. During hurricanes, the power spectra over sea were higher than those on open land and cospectral values over the two surfaces were comparable. The values of power spectra and cospectra are comparable for different wind speeds [8]. In general, up to now, there is still a lack of understanding of discrepancies and the underlying mechanism of turbulent characteristics over different underlying surfaces due to a lack of direct turbulent measurements during typhoons [4,9,10].

Many studies have evaluated the applicability of Monin–Obukhov similarity theory (MOST) [11] in an offshore, onshore, or land environment [12,13], and a detailed re-evaluation is beyond the scope here. This study focuses on the comparison of turbulent characteristics in different environments rather than assessing the applicability of MOST or adjusting the fitting parameters of functions. The purpose of this work is to reveal the turbulence characteristics on different underlying surfaces (land, island, and sea surface) during (including before and after) typhoons. Atmospheric stability, turbulent spectra, friction velocity, turbulent kinetic energy, dissipative heating, and gust factor are compared here. For brevity, during (including before and after) typhoons is hereafter referred to as during typhoons.

The 10 Hz high-frequency turbulent measurements were collected during seven typhoons. Five typhoon events (Nockten in 2011, Nesat in 2011, Rammasun in 2014, Hato in 2017, and Mangkhut in 2018) were collected at an offshore tower (Figure 1a), two typhoon events (Hagupit in 2008 and Chanthu in 2010) were collected at a tower on an island (Figure 1b), and two typhoon events (Hato in 2017 and Mangkhut in 2018) were collected at a tower on land (Figure 1b). Due to the practical difficulties of instrumenting the sea surface in typhoon conditions, the data during typhoons were very deficient, and different typhoon events were captured on different observational towers. Because this study mainly focuses on the turbulence characteristics with wind speed on different surfaces, rather than the impact of typhoon structure on turbulence characteristics, we infer that the different typhoon events on the different surfaces have no significant impact on the results. Sections 2 and 3 present the experimental setup and characteristics of the typhoons, respectively. Sections 4 and 5 introduce the methodology and data processing, respectively. Section 6 shows the results. Discussions and conclusions are summarized in Section 7.

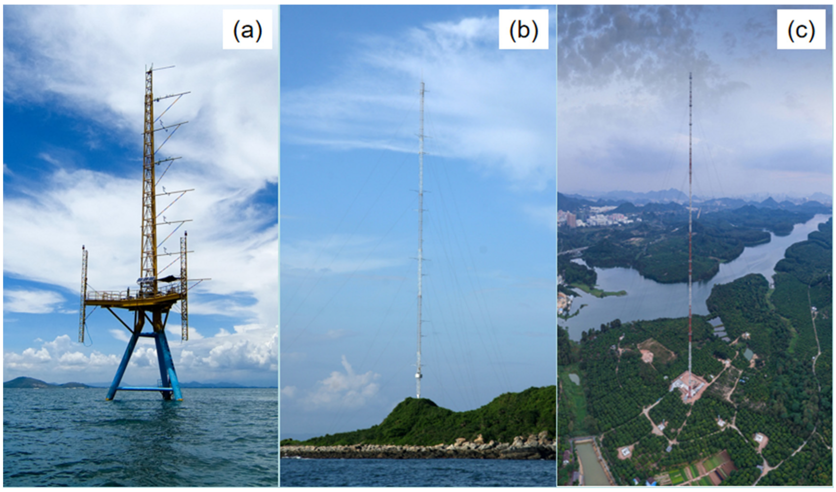

Figure 1. The snapshots of (**a**) the tower over sea, (**b**) the tower on island, and (**c**) the tower on land.

2. Experimental Setup

The three orthogonal wind components at a frequency of 10 Hz were collected at three research towers during seven typhoons from 2008 to 2018. Figure 1 shows the snapshots of the three towers. Their locations are shown in Figure 2. The tower over sea and the tower on the island stand along the shore-normal line in the South China Sea, 6.5 km and 4.5 km offshore, respectively. The distance between them is 2 km. They are 291 km away from the tower on land, which is about 10 km away from the nearest southwest coastline.

The tower over sea in Figure 1a is a 25 m high steel tower on an integrated marine meteorological observation platform in the South China Sea. The platform is about 11 m above the mean sea level (msl). It is operated by the Guangzhou Institute of Tropical and Marine Meteorology, China Meteorology Administration (CMA) [14]. The tower stands at a water depth of 15 m in the South China Sea (21.45° N, 111.37° E), and is 6.5 km away from the nearest northwest coastline. The Gill Windmaster Pro three-dimensional ultrasonic anemometers are installed on 2.0 m booms to the east of the tower facing the seaward direction at 27.3 m and 35.1 m above msl. The RM Young/05106 wind sensors are mounted on 2 m booms on five different planes (13.4 m, 16.4 m, 20.0 m, 23.4 m, and 31.3 m above msl) with a sampling frequency of 1 min. The 10 Hz three orthogonal wind components were collected at a height of 35.1 m during Typhoons Nockten (2011) and Nesat (2011) and at a height of 27.3 m during Typhoons Rammasun (2014), Hato (2017) and Mangkhut (2018).

The tower on the island shown in Figure 1b is a 100 m high meteorological observation tower with a guyed structure. It was operated by the Guangdong Climate Centre. The tower stands on a small island named Zhizai (21.45° N, 111.37° E), and is 4.5 km away from the nearest northwest coastline. The island area above the water is approximately 90 m × 40 m and is covered with sand and sparse weeds. The tower is about 10 m above msl [15]. The Gill Windmaster Pro three-dimensional ultrasonic anemometers are deployed on 2.5 m booms to the east of the tower facing the seaward direction, at a height of 60 m during Typhoon Hagupit (2008) and 40 m during Typhoon Chanthu (2010). The NRG #40 wind sensors are deployed on 2.5 m booms on six levels (10.0 m, 20.0 m, 40.0 m, 60.0 m, 80.0 m, and 100.0 m above msl) with a sampling frequency of 1 min.

The tower on land shown in Figure 1c is a 356 m high meteorological observation tower with a hollow steel structure. It was constructed in 2016 and is operated by the Meteorological Bureau of Shenzhen Municipality. The tower stands in the Tiegang Reservoir Water Reserve in Shenzhen, China (22.65° N, 113.90° E), and is about 10 km away from the nearest southwest coastline. The topography and terrain map around the tower as shown in Figure 2 in Luo et al. [16] illustrates that the underlying surface around the tower is relatively smoother than nearby suburban/forest areas. To its north and east, there is mostly cropland or water within 1–2 km and farther away are 10–30 m low-rise buildings, mixed with forest areas. To its south and west, there are mainly woods and lakes within 5 km. The four three-dimensional ultrasonic anemometers (denoted as CSAT3, Campbell Scientific Inc., Logan, UT, USA) are mounted at the northern end of 3.8 m north-south overhanging beams at four different planes (10, 40, 160, and 320 m above ground level).

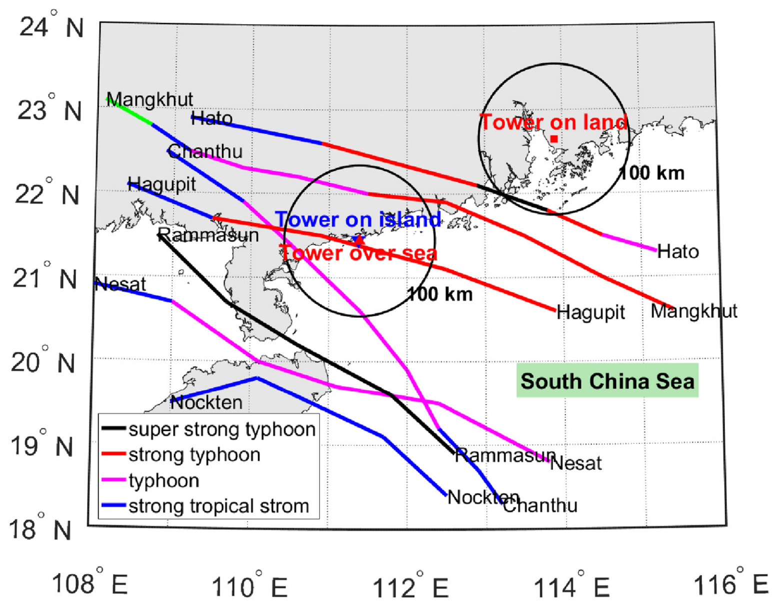

Figure 2. The tracks of the typhoons along with the locations of the three observation towers. The red upward-pointing triangle denotes the tower over sea corresponding to Figure 1a, the blue downward-pointing triangle denotes the tower on the island corresponding to Figure 1b, and the red square denotes the tower on land corresponding to Figure 1c. The distance between the tower over sea and the tower on the island is about 2 km, so their signs largely overlap each other. The black circles show the distance to the towers of 100 km. The different color lines mark the different typhoon categories. Super strong typhoon is larger than 51 m s^{-1}, and then 41.4~51 m s^{-1}, 32.7~41.4 m s^{-1}, and 24.5~32.7 m s^{-1} follow. The typhoon track and typhoon intensity data are from the website http://tcdata.typhoon.org.cn/ (accessed on 1 August 2022) [17].

3. Characteristics of the Typhoons

Figure 2 shows the seven typhoon tracks along with the locations of the three observation towers. Detailed information on the typhoons is listed in Table 1. Only the super strong Typhoon Hato (2017) and the strong Typhoon Mangkhut (2018) tracked between the tower on land and the tower over sea and were recorded simultaneously at the two towers on land and over sea.

Table 1. Information of the data during the seven typhoon events.

Typhoon	Time Period	The Closest Distance to the Tower at Sea/the Tower on Land (km)	Central Pressure (hPa)	Tower over Sea		Tower on Island		Tower on Land	
				Instrument Height (m)	Max u_{10} (m s^{-1})	Instrument Height (m)	Max u_{10} (m s^{-1})	Instrument Height (m)	Max u_{10} (m s^{-1})
Hagupit	23–24 September 2008	0	940	×	×	60	23.8	×	×
Chanthu	21–23 July 2010	65	970	×	×	40	32.1	×	×
Nockten	29–30 July 2011	220	980	35.1	18.7	×	×	×	×
Nesat	29–30 September 2011	195	950	35.1	25.7	×	×	×	×
Rammasun	18–19 July 2014	160	910	27.3	23.4	×	×	×	×
Hato	22–25 August 2017	137/95	935	27.3	15.1	×	×	10, 40, 160, 320	11.1
Mangkhut	15–18 September 2018	63/134	945	27.3	21.7	×	×	10, 40, 160, 320	10.7

×: no data are available.

Typhoon Hato underwent a rapid intensification over the shallow water in the South China Sea before making landfall. Typhoon Mangkhut was already a super typhoon over the Pacific Ocean and retained the category until the day after landfall. Typhoon Mangkhut had a wider circulation and larger wind footprint than Typhoon Hato. Figures 3 and 4 show 10 min average wind speed time series and distances to the towers of Typhoons Hato and Mangkhut, respectively. The wind speeds recorded at different heights on the tower over sea are in good agreement and continuity. The wind speeds recorded on the tower on land increase with height. Due to the influence of rainfall, the recorded available quality-controlled maximum 10 min average wind speed at a height of 10 m (u_{10}) is only 11.1 m s^{-1} and 10.7 m s^{-1} on the tower on land during Typhoon Hato and Typhoon Mangkhut, respectively, though the distance of their center to the tower on land is only 95 km and 134 km, respectively.

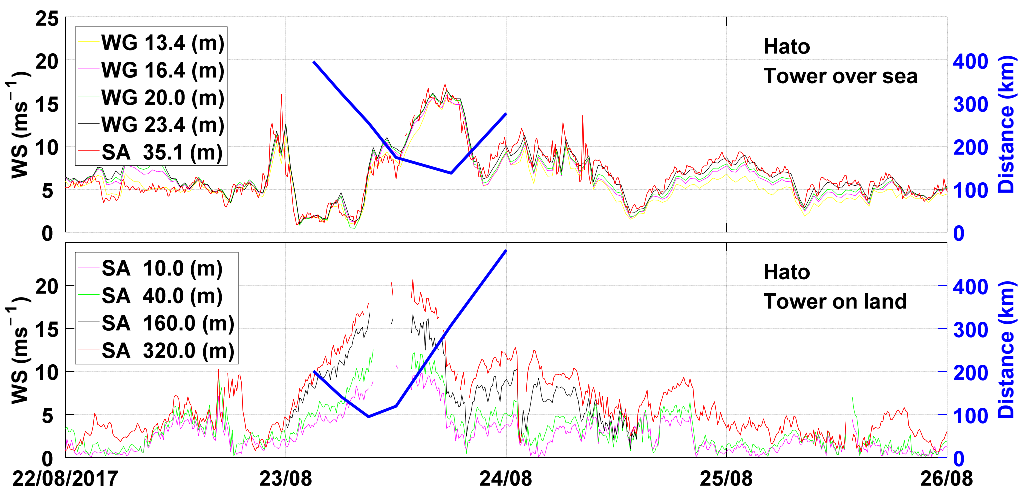

Figure 3. The raw 10 min average wind speed (WS) and the distance of the typhoon center to the tower (data obtained from the website http://tadata.typhoon.org.cn/) (accessed on 1 August 2022) [17] during Typhoon Hato. (**top**) The WS observations derived from the sonic anemometer (SA) and the standard wind gauges (WG) at the tower over sea and (**bottom**) the data derived from the sonic anemometers (SA) at the tower on land.

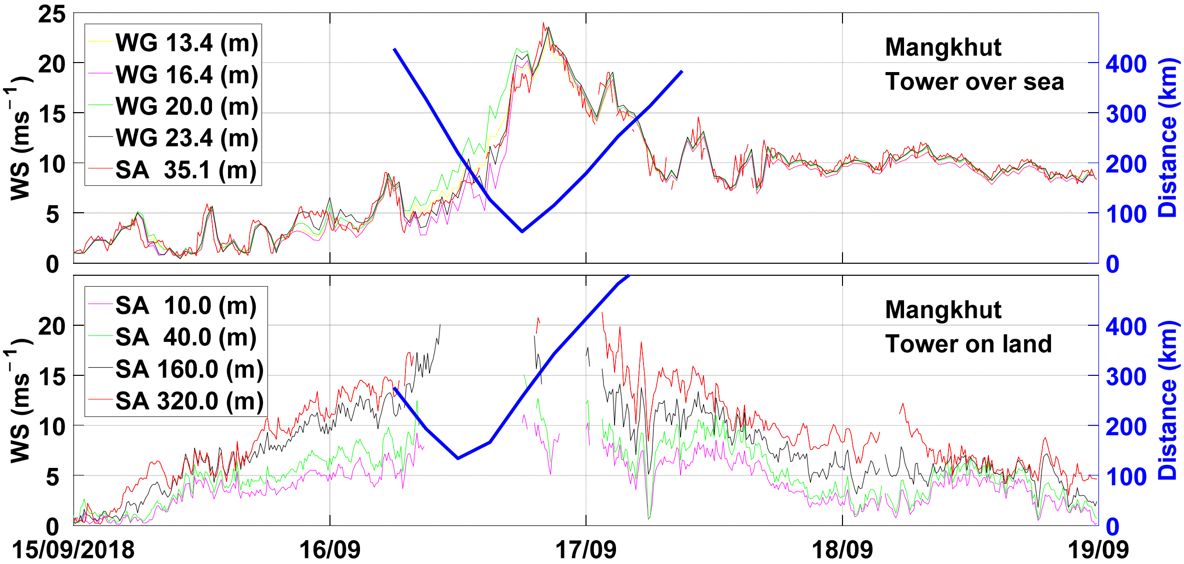

Figure 4. The same as Figure 3 except for that during Typhoon Mangkhut.

A detailed description of the other five typhoons (Hagupit, Chanthu, Nesat, Nockten, and Rammasun) can be found in Bi et al. [18]. Their 10 min wind speed time series, as shown in Figure 3 in Bi et al. [18], also had good agreement and continuity. The strong Typhoon Hagupit moved almost directly over the tower on the island and had the maximum recorded 10 min average wind speed of 47 m s^{-1} at a height of 60 m. The other four typhoons passed to the south of the towers. Typhoons Hagupit and Chanthu were recorded at the tower on the island. Typhoons Nockten, Nesat, and Rammasun were recorded at the tower over sea. Due to the high-frequency data being sensitive to rainfall and other sampling uncertainties, the highest u_{10} of 32 m s^{-1} from quality-controlled high-frequency data were recorded during Typhoon Chanthu instead of the other stronger typhoons.

4. Methodology

4.1. Atmospheric Stability Parameter

Based on the Monin-Obukhov similarity theory [11,19], atmospheric stability can be characterized by the inverse of Monin-Obukhov length (L).

$$L = -\frac{u_*^3 \overline{\theta}_0}{gk\overline{w'\theta_v'}} \tag{1}$$

where g denotes the gravitational acceleration, $\overline{w'\theta_v'}$ indicates the flux of virtual potential temperature, and $\overline{\theta}_0$ indicates the mean potential temperature.

The dimensionless height $\zeta = z/L$ is used as an atmospheric stability parameter, where $\zeta < 0$ denotes unstable, $\zeta > 0$ is stable, and $\zeta \approx 0$ is neutral conditions.

4.2. Friction Velocity (u_*)

Based on the eddy covariance method, the u_* is defined by [20]:

$$u_* = \left(\left(\overline{u'w'}\right)^2 + \left(\overline{v'w'}\right)^2 \right)^{1/4} \tag{2}$$

where u', v', and w' indicate turbulent fluctuations of three wind components. The overbar denotes Reynolds averaging.

4.3. Turbulent Kinetic Energy (TKE)

Based on the high-frequency turbulent observations, the TKE is calculated by [20]:

$$TKE = \frac{1}{2}\left(\overline{u'^2} + \overline{v'^2} + \overline{w'^2}\right) \tag{3}$$

4.4. Dissipative Heating (DH)

According to the method proposed by Bister and Emanuel [21], the DH is calculated by the following formula:

$$DH = \rho C_D \overline{u}^3 \tag{4}$$

where ρ is the air density.

Similarly, to have a comparison between those from different measurement heights, the 10 m DH is estimated by:

$$DH = \rho C_{D10} \overline{u}_{10}^3 \tag{5}$$

4.5. Gust Factor (GF_u)

Gust factor is a ratio of gust to average wind speed [22]:

$$GF_u(\tau, T) = \frac{\overline{u}_{max,\tau}}{\overline{u}_T} \tag{6}$$

where gust $\overline{u}_{max,\tau}$ indicates the largest τ-averaged wind speed with T minutes. $\overline{u}_T$ is the T minutes average wind speed. The WMO recommends that the gust is defined as the maximum 3 s average during a 10 min sampling period [23]. So τ = 3 s and T = 10 min are applied here.

5. Data Processing and Quality Control

The sonic anemometer measurements are processed by using the same method reported in Bi et al. [18]. Spike detection and removal are similar to that of *Hojstrup* [24]. Based on the Ogive method [25], the 10 min average is judged to be an optimal averaging period for calculating turbulent fluxes [18]. According to the comparison between double rotation and planar-fit rotation, the double coordinate rotation is selected for eliminating the instrument tilt errors [26,27]. In order to ensure the data quality, the 10 min average wind speeds yielded from the sonic anemometers are compared with those recorded from the slow response sensors mounted at the same towers, and sonic anemometer measurements with a difference of >5% are discarded in further analysis. In order to minimize the influence of flow distortion by the tower, the data over sea and on the island with wind directions between 240° and 300° are excluded, and the data on land with wind directions between 150° and 210° are excluded. Additionally, Bi et al. [18] have demonstrated by footprint analysis that the sonic anemometer measurements from the tower over sea and on the island are not influenced by either the island or the shore.

6. Results

6.1. Atmospheric Stability

Atmospheric stability is the state of the atmosphere related to either promoting or suppressing vertical air motion. Essentially, unstable atmospheres tend to promote vertical updrafts and stable atmospheres tend to suppress vertical updrafts. It is a crucial variable in surface layer parameterization in numerical weather prediction models, and is also important for cloud formation and precipitation, wind energy generation, atmosphere turbulence intensity, dilution of air pollutants, etc. Figure 5 shows the percentage of occurrence of the dimensionless stability parameter (ζ) over sea, on the island, and on land; here, the stability classification is according to the definition classes for ζ shown in Table 2 [28].

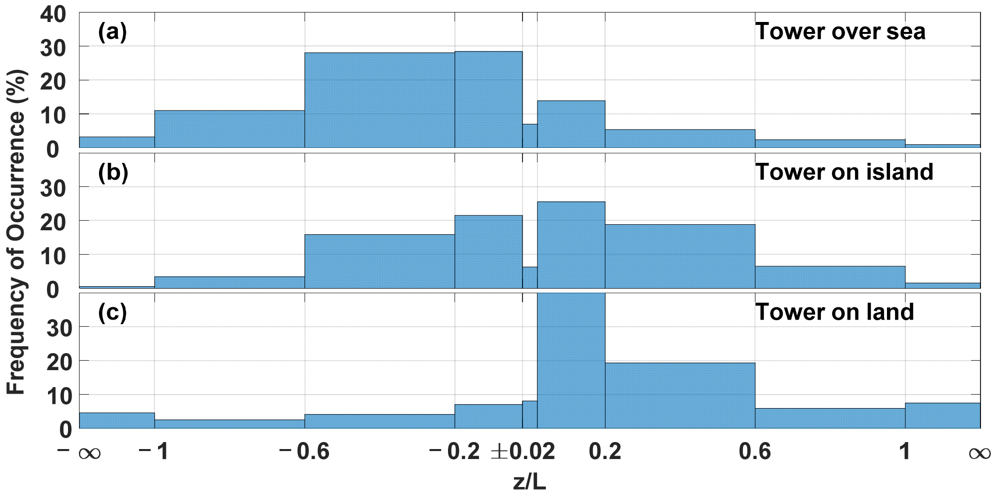

Figure 5. The percentage of occurrence of the dimensionless stability parameter $\zeta = z/L$ (**a**) at the tower over sea, (**b**) at the tower on the island, and (**c**) at the tower on land. The value of $z/L < -1$ indicates extremely unstable; $-1 < z/L < -0.6$, very unstable; $-0.6 < z/L < -0.2$, unstable; $-0.2 < z/L < -0.02$, weakly unstable; $-0.02 < z/L < 0.02$, nearly neutral; $0.02 < z/L < 0.2$, weakly stable; $0.2 < z/L < 0.6$, stable; $0.6 < z/L < 1$, very stable; $z/L > 1$, extremely stable.

Table 2. Stability classification method same as Sorbjan and Grachev [28].

Stability Class	ζ	Stability Class	ζ	Stability Class	ζ
extremely unstable	$\zeta < -1$	weakly unstable	$-0.2 < \zeta < -0.02$	stable	$0.2 < \zeta < 0.6$
very unstable	$-1 < \zeta < -0.6$	nearly neutral	$-0.02 < \zeta < 0.02$	very stable	$0.6 < \zeta < 1$
unstable	$-0.6 < \zeta < -0.2$	weakly stable	$0.02 < \zeta < 0.2$	extremely stable	$\zeta > 1$

Figure 5 illustrates that the unstable condition dominates on the ocean surface, the proportions of unstable and stable conditions are nearly the same on the island surface, and the stable condition dominates on the land surface. The proportions of near-neutral conditions of 6.4~7.0% are close on the three surfaces. The unstable conditions are 72.7%, 41.4%, and 23.0% on the ocean, on the island, and on the land surface, respectively. The stable conditions are 20.3%, 51.9%, and 70.6% on the ocean, on the island, and on the land surface, respectively. The total percentage of occurrence of extremely unstable and extremely stable conditions on the land surface is 13.9%, which is significantly greater than that of 3.9% and 2.4% on the ocean and island surfaces. Our measurements fit well with those previously reported [5,6]. They showed that the marine air below 50 m is mostly in an unstable condition compared to the stability above, inferring the presence of an internal marine boundary layer. Additionally, it is expected that the stable conditions over offshore tower are mainly coming from the land.

6.2. Spectra Analysis

Atmospheric energy spectrum means the distribution of atmospheric energy with frequency. Energy spectrum analysis can intuitively reflect the composition scale of energy. Figures 6 and 7 show the consecutive 1 h average power spectrum and cospectra of the along-wind velocity during typhoons, respectively. The black line and the magenta line stand for the results over sea and on the island, respectively. Other color lines denote the results at different heights on land. The measurements over sea, on the island, and on land (40 m) with similar wind speed are selected. Those at different heights on land use the same time period measurements.

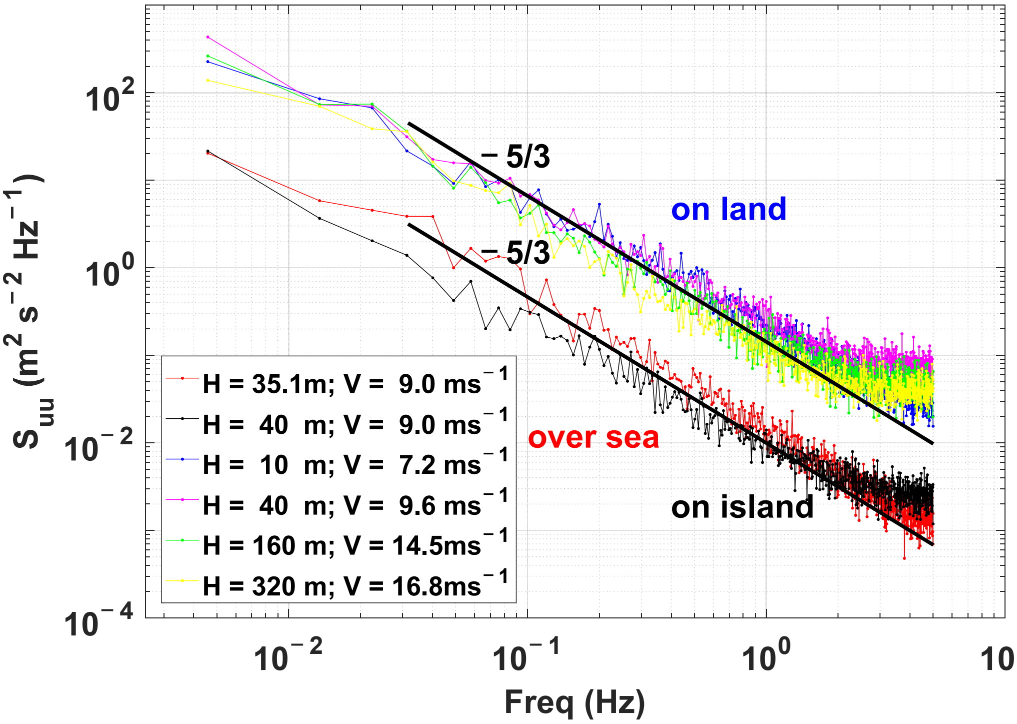

Figure 6. The power spectral density of the along-wind velocity during typhoons. The different color lines represent the measurements in different environments. The yellow, green, red, and blue lines show the measurements collected at the tower on land at 8:00 on 23 August 2017 during Typhoon Hato. The magenta line stands for the measurements collected at the tower on the island at 14:00 on 21 July 2017 during Typhoon Chanthu. The black line shows the measurements collected at the tower over sea at 23:00 on 28 September 2011 during Typhoon Nesat. The black lines are the 5/3 slope.

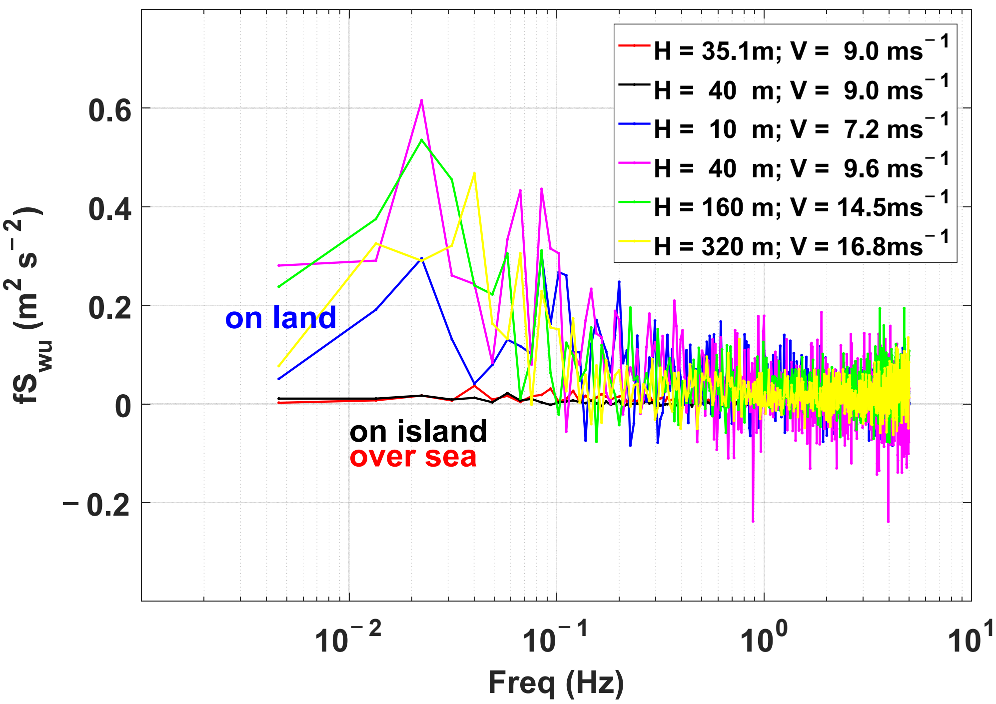

Figure 7. The same as Figure 6 except for cospectra of along-wind momentum flux.

Figures 6 and 7 show the very similar shape of the power spectral and cospectral density of the along-wind velocity over sea and on the island. Those spectral shapes at different heights on land also show almost overlapping curves. That means that the different wind speeds (different observation heights) do not affect the distribution shape of the spectrum. Figure 6 confirms the robust canonical shape of Kolmogorov's power law with the $-5/3$ slope, and the inertial subrange at high frequency can be resolved. The turbulent energy on land is considerably higher than those over sea (island). Figure 7 shows that the cospectra on land are more peaked than those over sea (island) in low frequency, in accord with previous results reported [4,8].

Note, the spectra and cospectra of cross-wind velocity and vertical-wind velocity are also plotted and the similar characteristics are depicted (not shown).

6.3. *Friction Velocity, Turbulent Kinetic Energy, and Dissipative Heating*

Bi et al. [18] have demonstrated that the relationships between turbulent variables (friction velocity) and wind speed do not exhibit a systematic variation with heights. So, we combined the observations at different heights and performed a composite analysis on the tower over sea and those on the tower on the island, respectively.

Friction velocity (u_*) is a key turbulence parameter to represent the overturning velocity of energy-containing eddies. Figure 8 shows u_* as a function of u_{10}. Figure 8 depicts that u_* increases with increasing u_{10} whether over sea, on the island, or on land. The values of u_* collected on both the tower over sea and the tower on the island have similar patterns. The increasing rate of u_* over sea (island) slows down when $u_{10} > 18$ m s^{-1}. The values of u_* collected at different heights on land have similar patterns. The values of u_* on land are much larger than those over sea. The cyan right-pointing triangle symbols are previous measurements on the Donghai island. The tower is 2.3 km inland from the coast line and is surrounded by farmland, woodland, and residential areas [29]. The measurements on the Donghai island are higher (lower) than those over sea (on land). This shows that u_* is higher on rougher surfaces.

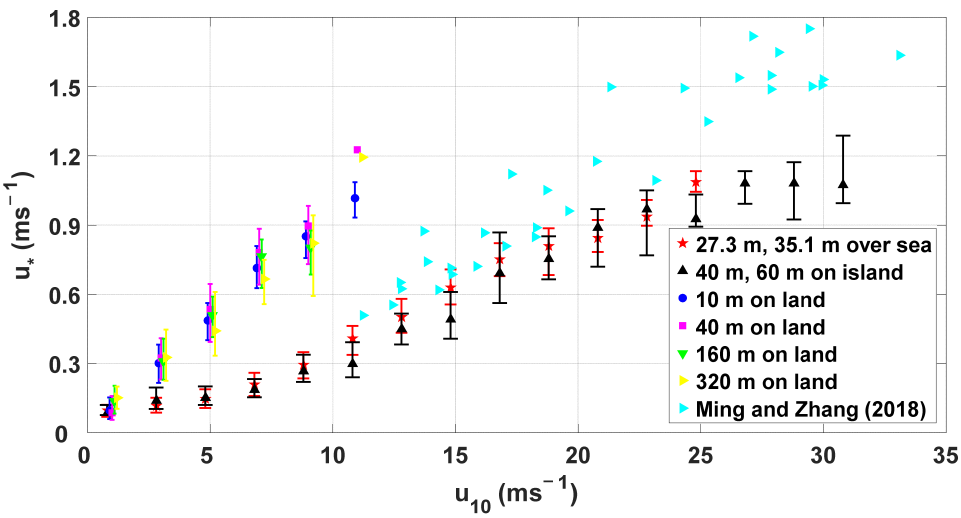

Figure 8. The values of the friction velocity (u_*) as a function of u_{10} during typhoon events. The symbols and bars represent the median values and interquartile ranges, respectively. The u_{10} bin size is 5 m s^{-1}. The red pentagram symbols denote the observations from the tower over sea. The black up-pointing triangle symbols denote the observations from the tower on island. Other color symbols show the observations from the tower on land at different heights. Moreover, the cyan right-pointing triangles shown for comparison represent the data points reported in Ming and Zhang [29].

Turbulent kinetic energy (TKE) is a measure of turbulence intensity. It explains the generation, maintenance, and dissipation of turbulence. Figure 9 shows the TKE as a function of u_{10}. Figure 9 depicts that TKE increases with increasing u_{10} whether over sea, on the island, or on land. The values of TKE collected on both the tower over sea and the tower on the island have similar patterns. The values of TKE collected at different heights on land have similar patterns. The major difference between those over sea (island) and those on land is the increasing rate of TKE with u_{10}. The TKE derived from the land increases quickly. When $u_{10} < 10$ m s^{-1}, the values of TKE over sea (island) are really small, far less than those on land. Similar to u_*, the measurements of TKE on the Donghai island are higher (lower) than those over sea (on land). This shows that the TKE is higher on rougher surfaces.

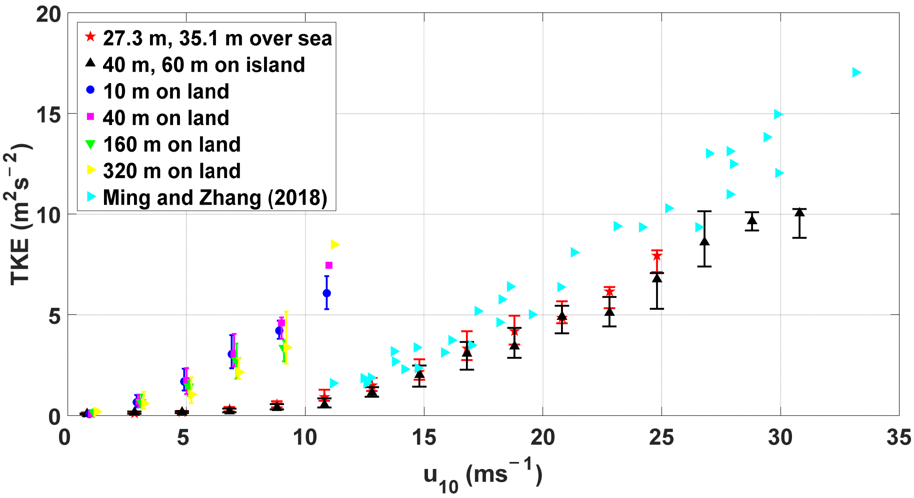

Figure 9. The same as Figure 8 except for the turbulent kinetic energy (TKE) as a function of u_{10}.

Dissipative heating (DH) is an important source of energy for typhoon development and intensification [21]. Most of the energy is dissipated through the molecular process in the air–sea (air–land) interaction, while a small part of the energy is returned to the atmosphere through dissipative heating. Figure 10 shows DH as a function of u_{10}. Figure 10 depicts that the DH increases with u_{10} in much the same manner as the turbulent kinetic energy (TKE). The values of DH increase with increasing u_{10} and those on land are much larger than those over sea (island). The values of DH at the heights of 160 m and 320 m are obviously larger than those at the heights of 10 m and 40 m on land. Figure 10 shows that DH is up to 40 W m^{-2} over sea (island) when $u_{10} \approx 30$ m s^{-1} and DH is up to 30 W m^{-2} on land when $u_{10} \approx 10$ m s^{-1}. The result over sea is actually consistent with previous studies [30]. Similar to u_* and TKE, the measurements of DH on the Donghai island are higher (lower) than those over sea (on land). This shows that the DH is higher on rougher surfaces.

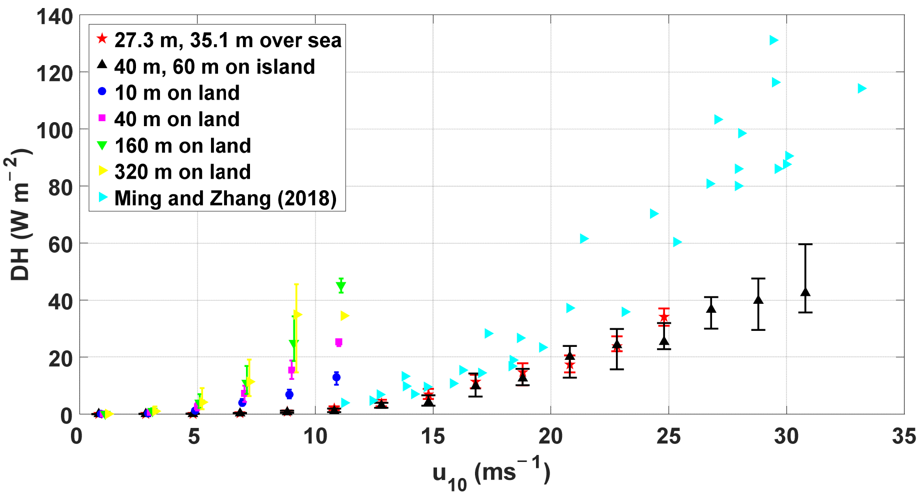

Figure 10. The same as Figure 8 except for the dissipative heating (DH) as a function of 10 m wind speed (u_{10}).

6.4. Gust Factor

Gust is the instantaneous wind speed, which is higher with larger fluctuations compared with the average wind speed. It is closely related to wind energy applications, aviation security, as well as damage to buildings and forests, etc. [23]. As described above, gust factor establishes the relationship between gust and average wind speed. Figure 11 shows the distribution probability of GF_u. Previous studies have shown that gust factor is sensitive to surface roughness and turbulent intensity [1,7]. Figure 11 shows that the width of the distributions of GF_u over sea and on the island are similar. The distribution shapes of GF_u on different underlying surfaces and at different heights on land are very different. The distributions widen and shift higher on land. The distributions at heights of 10 m and 40 m are biased to higher values than those at heights of 160 m and 320 m on land. The heights of 160 m and 320 m are above the surface layer.

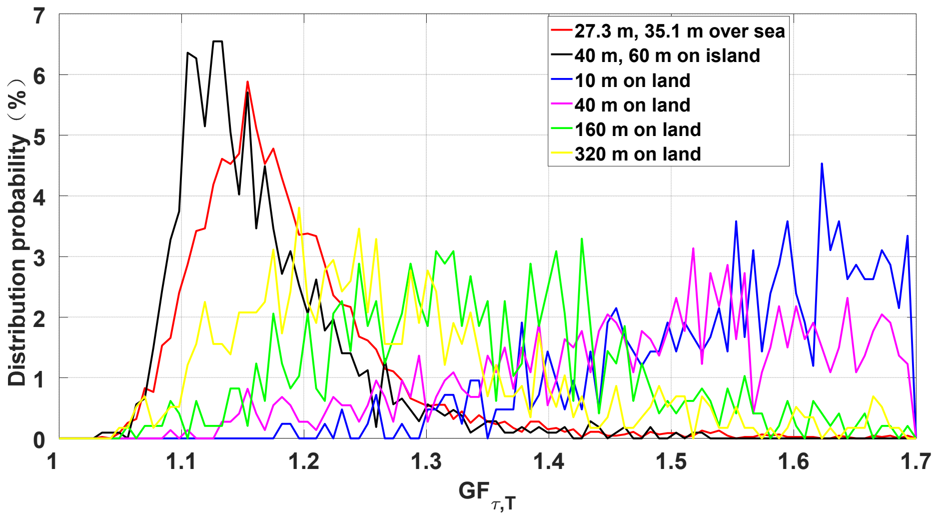

Figure 11. Distribution probability of GF_u with gust averaged time τ = 3 s and wind speed averaged time T = 10 min.

7. Conclusions and Discussions

Based on the 10 Hz high-frequency turbulent measurements collected over different underlying surfaces during seven typhoons, atmospheric stability, turbulent spectrum, friction velocity, turbulent kinetic energy, dissipative heating, and gust factor are compared here. The towers over sea and on the island are placed in areas of 15 m and 10 m water depths along a shore-normal line, 6.5 km and 4.5 km offshore, respectively. The tower on land stands in a reservoir 10 km away from the coastline and is about 290 km away from the towers over sea (island). The turbulent variables studied here show a similar shape over sea and on the island. The size of the island is really small and observation heights are 40 m and 60 m, which makes the fetch of measurements mainly coming from the sea surface. Actually, the footprint analysis in our previous work also supports this inference that the measurements of turbulence during typhoons on the island mainly represent the sea surface [18]. The turbulent variables at 160 m and 320 m are different from those at 10 m and 40 m on land. This is probably because 160 m and 320 m are above the surface layer, so different turbulent characteristics shown there.

The turbulent characteristics are very different over sea and on land because of the different underlying surface roughness; land surface is rougher than sea surface. The turbulent variables on land are larger than those over sea at the same wind speed. The unstable condition dominates on the ocean surface, the proportions of unstable and stable conditions are nearly the same on the island surface, and the stable condition dominates on the land surface. This is similar to previous results [5,6] and reveals a little influence of the island on the measurements on the island still exists; spectral analysis confirms the robust canonical shape of Kolmogorov's power law with the $-5/3$ slope, and the inertial subrange at high frequency can be resolved. The turbulent energy on land is considerably higher than that over sea. The cospectra on land are more peaked than those over sea; all of the friction velocity, turbulent kinetic energy, and dissipative heating increase with increasing 10 m wind speed and those on land are much larger than those over sea. The distributions of gust factors widen and shift higher on land than those over sea. The distributions of gust factors at heights of 10 m and 40 m are biased to higher values than those at heights of 160 m and 320 m on land.

Although still limited, the results reveal some discrepancies of turbulent characteristics over sea and on land during typhoons. More measurements and analysis are needed to confirm the findings.

Author Contributions: Conceptualization, X.B. and C.L. (Chunxia Liu); methodology, X.B., C.L.(Chao Lu) and Z.Z.; software, X.B. and J.H; validation, H.Y. and Q.S.; formal analysis, X.B. and C.L. (Chunxia Liu); investigation, X.B., C.L. (Chunxia Liu), J.H. and Z.Z.; resources, J.H. and C.L. (Chao Lu); data curation, X.B., C.L. (Chao Lu) and J.H.; writing—original draft preparation, X.B.; writing—review and editing, X.B., C.L. (Chao Lu), C.L. (Chunxia Liu), J.H., H.Y., Z.Z. and Q.S.; visualization, X.B. and C.L. (Chao Lu); supervision, C.L. (Chunxia Liu) and Q.S.; project administration, X.B. and C.L. (Chunxia Liu); funding acquisition, X.B., C.L. (Chunxia Liu) and Z.Z. All authors have read and agreed to the published version of the manuscript.

Funding: This study was funded by the Key Research and Development Projects in Guangdong Province (2019B111101002), the National Natural Science Foundation of China (Grant No. 41675019, 41875021, and 41830533) and the Funding of Guangdong Meteorological Service (GRMC2020M29). And The APC was funded by the National Natural Science Foundation of China (Grant No. 41675019).

Institutional Review Board Statement: Not applicable.

Informed Consent Statement: Not applicable.

Data Availability Statement: The data that support the findings of this study are available on request from the corresponding author. The data are not publicly available due to them containing information that could compromise research participant privacy.

Acknowledgments: The authors thank all the crew members of the Marine Meteorological Science Experiment Base at Bohe and the Shenzhen National Climate Observatory for their help in conducting the campaigns and collecting the valuable data. We thank the Shenzhen National Climate Observatory, Meteorological Bureau of Shenzhen Municipality for providing measurements. The authors would like to also thank Zhiqun Shi and Wenchao Chen of the Guangdong Climate Centre for their help with the data on the tower on the island.

Conflicts of Interest: The authors declare no conflict of interest.

References

1. Pryor, S.C.; Conrick, R.; Miller, C.; Tytell, J.; Barthelmie, R.J. Intense and extreme wind speeds observed by anemometer and seismic networksAn eastern U.S. case study. *J. Appl. Meteor. Climatol.* **2014**, *53*, 2417–2429. [CrossRef]
2. Suomi, I.; Vihma, T.; Gryning, S.-E.; Fortelius, C. Windgust parametrizations at heights relevant for wind energy: A study based on mast observations. *Quart. J. Roy. Meteor. Soc.* **2013**, *139*, 1298–1310. [CrossRef]
3. Garratt, J. *The Atmospheric Boundary Layer*; Cambridge University Press: Cambridge, UK, 1994; pp. 316–335.
4. Santana, R.A.; Dias-Júnior, C.Q.; do Vale, R.S.; Tóta, J.; da Silva, R.; Tapajós, R.; Manzi, A.O.; Beldini, T.P. Comparing the Air Turbulence above Smooth and Rough Surfaces in the Amazon Region. *Atmosphere* **2021**, *12*, 1043. [CrossRef]
5. Argyle, P.; Watson, S.J. Assessing the dependence of surface layer atmospheric stability on measurement height at offshore locations. *J. Wind. Eng. Ind. Aerodyn.* **2014**, *131*, 88–99. [CrossRef]
6. Platis, A.; Hundhausen, M.; Lampert, A.; Emeis, S.; Bange, J. The Role of Atmospheric Stability and Turbulence in Offshore Wind-Farm Wakes in the German Bight. *Bound. -Layer Meteorol.* **2022**, *182*, 441–469. [CrossRef]
7. Balderrama, J.A.; Masters, F.J.; Gurley, K.R. Peak factor estimation in hurricane surface winds. *J. Wind Eng. Ind. Aerodyn.* **2012**, *102*, 1–13. [CrossRef]
8. Moraes, O.L.; Fitzjarrald, D.R.; Acevedo, O.C.; Sakai, R.K.; Czikowsky, M.J.; Degrazia, G.A. Comparing spectra and cospectra of turbulence over different surface boundary conditions. *Phys. A-Stat. Mech. Its Appl.* **2008**, *387*, 4927–4939. [CrossRef]
9. Møller, M.; Domagalski, P.; Sætran, L.R. Comparing abnormalities in onshore and offshore vertical wind profiles. *Wind Energ. Sci.* **2020**, *5*, 391–411. [CrossRef]

10. Ryu, G.H.; Kim, Y.-G.; Kwak, S.J.; Choi, M.S.; Jeong, M.-S.; Moon, C.-J. Atmospheric Stability Effects on Offshore and Coastal Wind Resource Characteristics in South Korea for Developing Offshore Wind Farms. *Energies* **2022**, *15*, 1305. [CrossRef]
11. Monin, A.S.; Obukhov, A.M. Basic laws of turbulent mixing in the atmosphere near the ground. *Tr. Akad. Nauk SSSR Geofiz. Inst.* **1954**, *24*, 163–187.
12. Edson, J.B.; Fairall, C.W. Similarity relationships in themarine atmospheric surface layer for terms in the TKE and scalarvariance budgets. *J. Atmos. Sci.* **1998**, *55*, 2311–2328. [CrossRef]
13. Holtslag, M.; Bierbooms, W.; van Bussel, G. Validation of surface layer similarity theory to describe far offshore marine conditions in the Dutch North Sea in scope of wind energy research. *J. Wind. Eng. Ind. Aerodyn.* **2015**, *136*, 180–191. [CrossRef]
14. Huang, J.; Chan, P.-W. Progress of Marine Meteorological Observation Experiment at Maoming of South China. *J. Trop. Meteorol.* **2011**, *17*, 418–429. [CrossRef]
15. Wang, B.; Song, L.; Chen, W. Drag Coefficient during Strong Typhoons. *Adv. Meteorol.* **2013**, *2013*, 8. [CrossRef]
16. Luo, Y.; Li, Q.; Chan, P.; He, Y. Observation of Typhoon Hato based on the 356-m high meteorological gradient tower at Shenzhen. *J. Wind Eng. Ind. Aerod.* **2020**, *207*, 104408. [CrossRef]
17. Ying, M.; Zhang, W.; Yu, H.; Lu, X.; Feng, J.; Fan, Y.; Zhu, Y.; Chen, D. An Overview of the China Meteorological Administration Tropical Cyclone Database. *J. Atmos. Oceanic Technol.* **2014**, *31*, 287–301. [CrossRef]
18. Zhao, Z.K.; Liu, C.X.; Li, Q.; Dai, G.F.; Song, Q.T.; Lv, W.H. Observed drag coefficients in high winds in the near offshore of the South China Sea. *J. Geophys. Res. Atmospheres* **2015**, *120*, 2015JD023172. [CrossRef]
19. Foken, T. 50 years of the Monin–Obukhov similarity theory. *Bound.-Lay. Meteorol.* **2006**, *119*, 431–447. [CrossRef]
20. Stull, R. Neutral Boundary Layer Similarity Relationship Lists. In *An Introduction to Boundary Layer Meteorology*; Stull, R., Ed.; Springer: Dordrecht, The Netherlands, 1988.
21. Bister, M.; Emanuel, K.A. Dissipative Heating and Hurricane Intensity. *Meteorol. Atmos. Phys.* **1998**, *65*, 233–240. [CrossRef]
22. Brasseur, O. Development and Application of a Physical Approach to Estimating Wind Gusts. *Mon. Weather. Rev.* **2001**, *129*, 5–25. [CrossRef]
23. Suomi, S.-E.; Floors, G.R.; Vihma, T.; Fortelius, C. On the vertical structure of wind gusts. *Quart. J. Roy. Meteor. Soc.* **2015**, *141*, 1658–1670. [CrossRef]
24. Hojstrup, J. A statistical data screening procedure. *Meas. Sci. Technol.* **1993**, *4*, 153. [CrossRef]
25. Lee, X.; Law, B.; Massman, W. *Handbook of Micrometeorology: A Guide for Surface Flux Measurement and Analysis*; Springer Science & Business Media: Dordrecht, The Netherlands, 2005.
26. Bi, X.Y.; Wen, B.; Zhao, Z.K.; Huang, J.; Liu, C.X.; Huang, H.J.; Mao, W.K.; Wen, G.H. Evaluation of corrections on turbulent fluxes obtained by eddy covariance method in high winds. *J. Trop. Meteorol.* **2018**, *24*, 176–184. [CrossRef]
27. Kaimal, J.C.; Finnigan, J.J. *Atmospheric Boundary Layer Flows: Their Structure and Measurement*; Oxford University Press: New York, NY, USA, 1994; p. 289.
28. Sorbjan, Z.; Grachev, A.A. An Evaluation of the Flux–Gradient Relationship in the Stable Boundary Layer. *Bound.-Layer Meteorol.* **2010**, *135*, 385–405. [CrossRef]
29. Ming, J.; Zhang, J.A. Direct measurements of momentum flux and dissipative heating in the surface layer of tropical cyclones during landfalls. *J. Geophys. Res. Atmos.* **2018**, *123*, 4926–4938. [CrossRef]
30. Zhang, J.A.; Zhu, P.; Masters, F.J.; Rogers, R.F.; Marks, F.D. On Momentum Transport and Dissipative Heating during Hurricane Landfalls. *J. Atmos. Sci.* **2011**, *68*, 1397–1404. [CrossRef]